

Cite this: DOI: 00.0000/xxxxxxxxxx

Coherent imaging and dynamics of excitons in MoSe₂ monolayers epitaxially grown on hexagonal boron nitrideKarolina Ewa Połczyńska,^a Simon Le Denmat,^b Takashi Taniguchi,^c Kenji Watanabe,^c Marek Potemski,^{a,d,e} Piotr Kossacki,^a Wojciech Pacuski,^a Jacek Kasprzak,^{a,b,f}

Received Date

Accepted Date

DOI: 00.0000/xxxxxxxxxx

Using four-wave mixing microscopy, we measure the coherent response and ultrafast dynamics of excitons and trions in MoSe₂ monolayers grown by molecular beam epitaxy on thin films of hexagonal boron nitride. We assess inhomogeneous and homogeneous broadenings in the transition spectral lineshape. The impact of phonons on the homogeneous dephasing is inferred via the temperature dependence of the dephasing. Four-wave mixing mapping, combined with the atomic force microscopy, reveals spatial correlations between exciton oscillator strength, inhomogeneous broadening and the sample morphology. The quality of coherent optical response of the epitaxially grown transition metal dichalcogenides becomes now comparable with the samples produced by mechanical exfoliation, enabling coherent nonlinear spectroscopy of innovative materials, like magnetic layers or Janus semiconductors.

1 Introduction.

We are witnessing an astonishing progress in the assembly of complex heterostructures based on monolayers of semiconducting transition metal dichalcogenides (TMDs), an iconic example being MoSe₂ placed between flakes of hexagonal boron nitride (hBN). The fabrication technology principally relies on mechanical exfoliation of thin films from van der Waals bulk crystals, similarly to the revolutionary extraction of graphene from graphite¹. This technique has enabled important discoveries in

the field of condensed matter physics to name a few: demonstrations of novel strongly-correlated electron systems², moiré quantum matter³, optical sensing of a quantum Hall effect⁴, non-hydrogenic Rydberg series of excitonic excitations⁵, high-harmonic optical generation^{6,7} and giant coherent nonlinear response^{8,9}. It also boosted developments toward future applications of these materials in optoelectronics¹⁰ and medicine¹¹. While the non-scalability of the exfoliation top-down approach is not an issue for the fundamental research, for which the proof-of-principle demonstrations are essential, it is a major roadblock on the academia-industry pathway of this field. In order to merge these novel materials with the semiconductor microelectronics, strain-free monolayer samples homogeneously covering wafers of a few cm diameter are required¹².

This can only be achieved by employing epitaxial techniques. The chemical vapor deposition of TMD layers, including monolayers, have been reported¹³ with post-growth processing improving the samples' quality¹⁴. Also molecular beam epitaxy of TMDs has been highlighted^{15,16}. The optical response of as-grown monolayers was dominated by the inhomogeneous broadening of the studied exciton transitions (EX), typically in a range of several tens meV. Moreover, the MBE growth of the materials incorporating transition metals: Mo, W, is particularly challenging owing to their low surface mobility. This causes their aggregation, especially when roaming on a rough surface, such that typically grains not exceeding 10 nm size were obtained on a commonly used SiO₂ substrate. On top of that, the epitaxy has a slow rate and requires high temperatures for sublimation, rendering it demanding. Recently, a breakthrough in this area has been achieved¹⁷: by using atomically flat and thin hBN layers, MoSe₂ monolayers with 85% of surface coverage were MBE-grown, homogeneously occupying terraces of several hundreds of μm . A step-like improvement of the optical response was achieved with exciton's photoluminescence line width below 10 meV and a suppressed distribution of the central transition energy, down to 0.16 meV. Importantly, good optical properties of the MBE-grown

^a Faculty of Physics, University of Warsaw, ul. Pasteura 5, 02-093 Warszawa, Poland
E-mail: karolina.polczynska@fuw.edu.pl

^b Univ. Grenoble Alpes, CNRS, Grenoble INP, Institut Néel, 25 rue des Martyrs, 38000 Grenoble, France

^c International Center for Materials Nanoarchitectonics, National Institute for Materials Science, 1-1 Namiki, Tsukuba 305-0044, Japan

^d Laboratoire National des Champs Magnétiques Intenses, CNRS-UGA-UPS-INS-EMFL, 25 Av. des Martyrs, 38042 Grenoble, France

^e CENTERA Labs, Institute of High Pressure Physics, PAS, PL-01-142 Warsaw, Poland

^f Walter Schottky Institut and TUM School of Natural Sciences, Technische Universität München, 85748 Garching, Germany

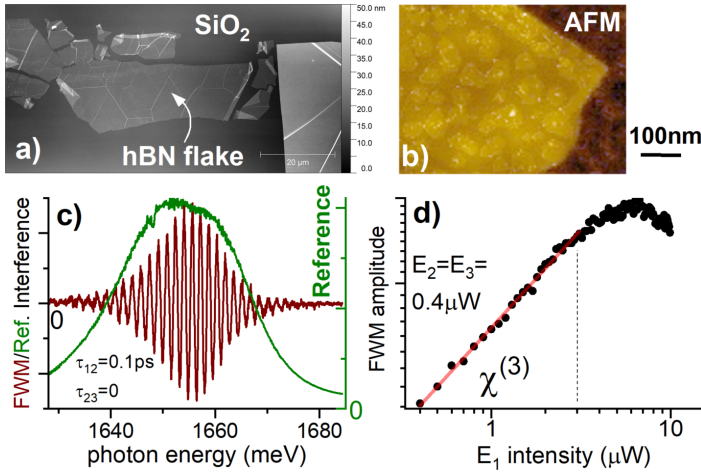


Fig. 1 Optical and structural characterization of the MBE-grown MoSe₂ monolayer. a) A large scale atomic force microscopy (AFM) image of the sample, showing the hBN flake on top of the SiO₂ substrate. b) The morphology of the sample revealed by the AFM performed with enhanced spatial resolution. The MoSe₂ monolayer flakes with a typical size of 100 nm grow on atomically flat terraces of the hBN. c) Four-wave mixing spectral interferogram (in red) measured at the exciton energy at T=5 K. The excitation pulse is given in green. d) Four-wave mixing intensity dependence. The linear regime of the FWM, also known as the $\chi^{(3)}$ regime, occurs for the driving powers up to $3 \mu\text{W}$. With increasing the excitation intensity, the onset of Rabi rotation is visible.

TMD are achieved without post-growth mechanical processing. Further to that, a heteroepitaxial growth of MoSe₂ monolayers on hBN, yielding wafer-scale van der Waals heterostructures of a good optical quality has recently been reported¹².

For optoelectronic applications, like ultrafast photodetectors, it is important to examine nonlinear absorption properties of these materials. In this work, we investigate the coherent optical response of these high quality epitaxial MoSe₂ monolayers using tools of nonlinear spectroscopy. By performing four-wave mixing (FWM) microscopy¹⁸, we assess the exciton's and trion's inhomogeneous σ and homogeneous γ line widths (FWHM). The impact of phonons on γ is evaluated by performing temperature dependence studies of the dephasing. Using FWM, we also measure the exciton density dynamics and find a longer population lifetime of trions with respect to excitons, as predicted in the literature^{19,20}. Next, by performing FWM spatial imaging we observe correlations between the FWM amplitude and σ .

2 Optical characterization

A large scale atomic force microscopy (AFM) image of the investigated sample is presented in Fig. 1 a. We concentrate on the macroscopic hBN flake, containing atomically flat terraces on several micron scale, which is deposited onto a SiO₂/Si substrate. The corresponding AFM image, measured with enhanced spatial resolution, is shown in Fig. 1 b. Therein, we recognize MoSe₂ monolayers with a typical size of around 100 nm, homogeneously covering the hBN, not yet affected by the grain coalescence process, required to obtain a complete monolayer¹⁷. Further AFM images are presented in Supplementary Fig. 8. The fabrication technology is described in Ref. [17]. The sample presented in

this work has been prepared in the following process: Before launching the MBE-growth, the substrate containing hBN flakes was degassed for 10 min at 750 deg C. Next, during 25 minutes of growth, we deposited a single monolayer of MoSe₂ at 300 deg C, and finally, we annealed the sample in Se flux for 2h at 750 deg C. Se was deposited from a standard effusion cell, Mo was deposited from the e-beam source with a Mo rod heated at one end by electrons. After the growth, there was no need for further processing of the sample to perform optical measurements.

The optical experiments were performed at T=5K, unless stated otherwise. In the photoluminescence, presented in the Supplementary Fig. 6, we observe the narrow emission lines of neutral excitons and charged excitons (trions), similarly as in Ref. [17]. The same exciton complexes are distinguished in white light reflectance. To infer the coherent response of these monolayers we perform FWM microscopy. We employ the same configuration of the setup as in Refs. [9,21]. On the sample surface, we focus three, colinearly polarized 100 fs pulses $\mathcal{E}_{1,2,3}$ generated by a Ti:Sapphire laser. $\mathcal{E}_{1,2,3}$ are spectrally centered at 750 nm, which is the expected wavelength of the exciton transition in MoSe₂ monolayers. By using acousto-optic deflectors operating around 80 MHz, we introduce distinct phase drifts (ϕ_1, ϕ_2, ϕ_3) within each of the triple-pulse sequence of the pulse train. In the reflected light, one can still differentiate and recover the amplitude and the phase of the pulses by homodyning and performing spectral interferometry with a reference pulse \mathcal{E}_R . Conversely, various nonlinear signals propagate at yet another frequencies within the reflected pulse train sequence. In particular, the FWM which is proportional to $\mathcal{E}_1^* \mathcal{E}_2 \mathcal{E}_3$, has a precisely defined phase $\phi_{\text{FWM}} = \phi_3 + \phi_2 - \phi_1$, which we detect by optical heterodyning. The resulting spectral interference of such heterodyned FWM with the \mathcal{E}_R is presented in Fig. 1 c. An example of the FWM spectrum, retrieved from the interferogram via spectral interferometry, is shown in the Supplementary Fig. 6 c. The signal-to-noise ratio is similar to previously studied bare monolayers obtained via mechanical exfoliation⁹. To remind, by measuring the FWM integrated amplitude as a function of the delay τ_{12} (τ_{23}) between the first (last) two arriving pulses, the dynamics of the excitonic coherence (density) is monitored — the relevant pulse sequences employed in our experiments are depicted at the top of Fig. 2 and Fig. 3, respectively.

At first, we take care to perform the experiments in the $\chi^{(3)}$ regime, in order to minimize excitation induced dephasing²¹ and local field effects. To check that, we carry out the FWM intensity dependence measurement²², presented in Fig. 1 d. We observe a purely linear increase of the FWM when increasing the \mathcal{E}_1 average power up to around $3 \mu\text{W}$, followed by the saturation and the onset of the local-field induced Rabi rotation. The following experiments have been therefore performed for $\mathcal{E}_1 = \mathcal{E}_2 = \mathcal{E}_3 < 1 \mu\text{W}$.

3 Coherence dynamics

The main advantage of FWM spectroscopy is its capability to accurately measure homogeneous, γ , and inhomogeneous, σ , contributions to the spectral line shape of the optical transition. By construction, there is a phase conjugation between the first order absorption induced by \mathcal{E}_1 and the FWM signal. In a presence

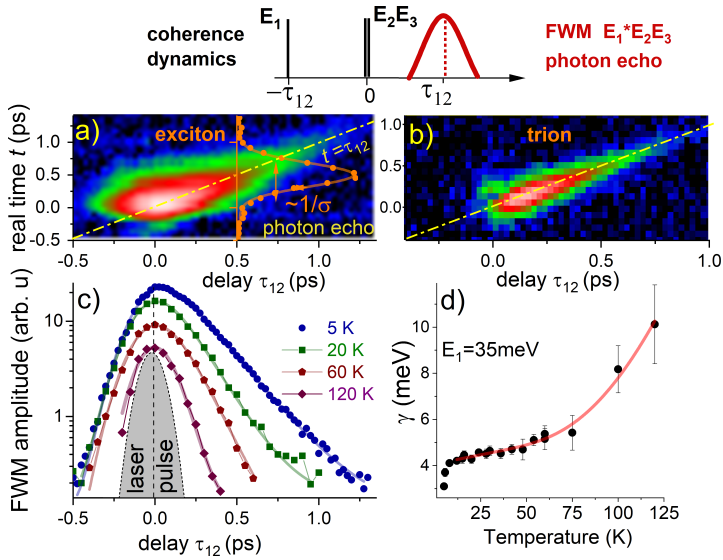


Fig. 2 Analysis of dephasing via four-wave mixing. Top: The pulse sequence employed to probe the coherence dynamics. a) Time-resolved four-wave mixing as a function of delay τ_{12} measured at the exciton transition displaying the photon echo. The temporal width of the echo yields the inhomogeneous broadening $\sigma_{\text{EX}} = 11.8 \text{ meV}$. b) as a) but measured at the trion transition. The pronounced echo yields $\sigma_{\text{TR}} = 30.4 \text{ meV}$. c) Exciton dephasing versus temperature as indicated, measured via time-integrated FWM. d) Resulting exciton homogeneous line width versus temperature. The red trace is the fit corresponding to a linear increase of γ due to interaction with acoustic phonons, followed by an exponential increase owing to the thermal activation of the optical phonons.

of σ , such conjugation generates the rephrasing and constructive interference in the FWM transient, known as photon echo, similar to the spin-echo phenomenon in nuclear magnetic resonance spectroscopy. From the decay of the echo as a function of τ_{12} one can measure the intrinsic dephasing time T_2 of the material and the homogeneous broadening (FWHM) $\gamma = 2\hbar/T_2$, whereas the temporal width of the echo yields σ .

We now thus analyse the exciton's spectral lineshape. The time-resolved FWM signal of the exciton is shown in Fig. 2 a. We observe the formation of a photon-echo: with increasing the delay τ_{12} , the maximum of the FWM transient shifts towards longer times t , such that the signal is aligned along the diagonal $t = \tau_{12}$ in the two-dimensional representation. The presence of σ , which quantifies the amount of electronic disorder, induces rephasing in the FWM transient, generating its Gaussian form, as depicted in orange. From the temporal FWHM of this Gaussian equal to $\delta_t = 363 \text{ fs}$ (corrected with respect to the pulse duration), we can calculate the spectral inhomogeneous broadening FWHM to be $\sigma_{\text{EX}} = 8\ln(2)\hbar/\delta_t = 11.8 \text{ meV}$. This value is consistent with the linewidth read from the FWM spectral interferogram, shown in Fig. 1 c.

Importantly, when the photon echo is developed, the time-integrated (TI) FWM amplitude as a function of τ_{12} is not sensitive to σ , but instead reflects the microscopic dephasing time T_2 , governing FWHM of the homogeneous broadening $\gamma = 2\hbar/T_2$. The blue circles in Fig. 2 c show such time-integrated FWM at $T=5\text{K}$. It is fitted with the exponential decay convoluted with the

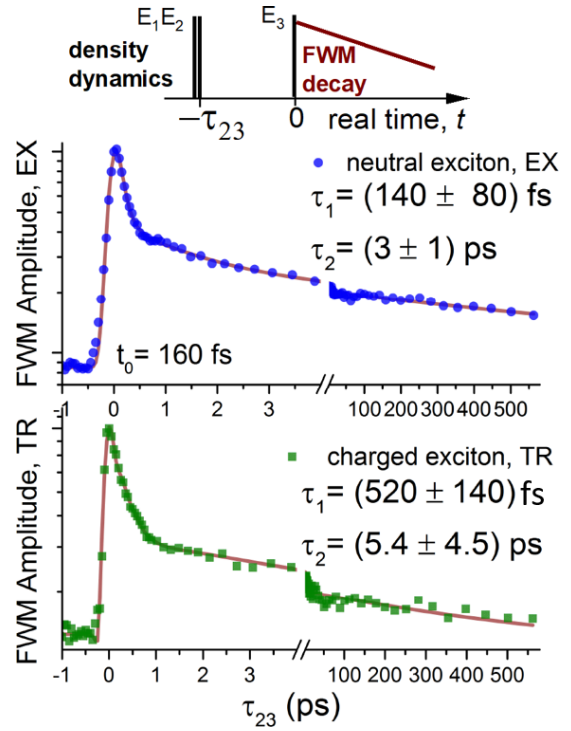


Fig. 3 Exciton and trion density dynamics measured via four-wave mixing. Top: a pulse sequence used to measure the density grating evolution via FWM, Middle (and bottom): Exciton (and trion) density dynamics showing a biexponential decay.

Gaussian, to account for a finite pulse duration, as represented in grey. For $\tau_{12} > 0$, an exponential decay is observed, yielding $\gamma_{\text{EX}}(5\text{K}) = 3 \text{ meV}$. This value is three times that measured on the bare MoSe_2 MLs⁹ and is also larger than in $\text{hBN}/\text{MoSe}_2/\text{hBN}$ heterostructures (produced via exfoliation and deterministic transfer methods) operating at the homogeneous limit²¹. We attribute such a rapid loss of the exciton coherence to the strong non-radiative processes in our MBE grown samples. Interestingly, we also observe the signal for $\tau_{12} < 0$: the FWM onset is detected noticeably earlier than expected from the finite pulse duration, especially bearing in mind a careful compensation of the temporal chirp in our experiments. From the exponential decay toward negative delays, we determine the coherence time due to the local field effect of approximately $T_{\text{LC}} = 0.1 \text{ ps}$.

In Fig. 2 b, we present analogous time-resolved FWM, but this time measured on the trion transition. We remark that the photon echo is even more pronounced, i.e. the FWM is yet more congregated along the diagonal, indicating a larger σ . Indeed, we here determine $\sigma_{\text{TR}} = 30.4 \text{ meV}$. Again, from the TI FWM (not shown) we determine $\gamma_{\text{TR}} = (7.7 \pm 0.2) \text{ meV}$. This larger value with respect to γ_{EX} is expected and consistent with recent measurements on exfoliated MoSe_2 ⁹ and past predictions and experiments on GaAs QWs¹⁹. We further notice lack of the signal for $\tau_{12} < 0 \text{ ps}$, due to a larger σ .

In Figs. 2 d we report the temperature dependence of γ_{EX} . We observe a linear increase of γ , due to a coupling with acoustic phonons. It is then followed by an exponential growth with an activation energy of 35 meV , well corresponding to the thermal

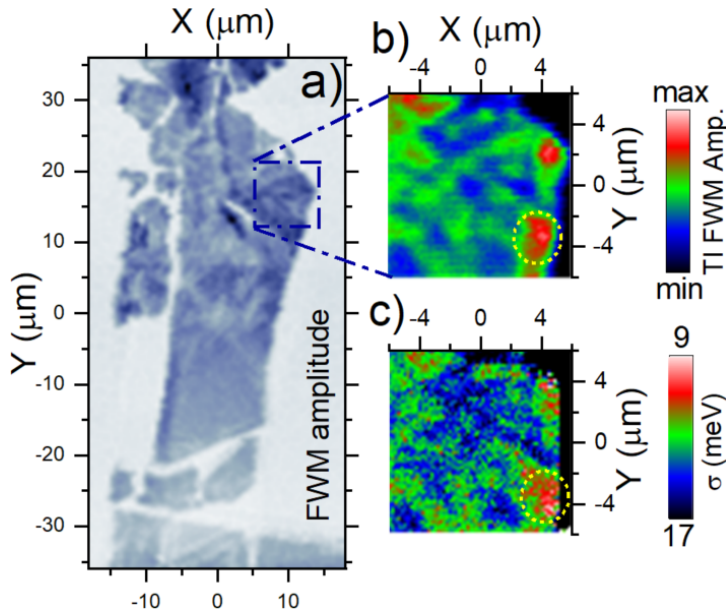


Fig. 4 Four-wave mixing imaging characteristics. a) Time-integrated FWM amplitude measured on a large area of $(36 \times 72) \mu\text{m}^2$ showing the strong signal generated at MoSe₂ monolayers grown on hBN. b) as a), but zoomed in, as indicated by the blue square. c) Spatial mapping of the spectral inhomogeneous broadening (FWHM) obtained from the temporal width of the photon echo. Areas generating a strong FWM in b) also display the lowest inhomogeneous broadening in c), as indicated by the yellow circle.

activation of optical phonons^{9,22}. This phonon induced dephasing is therefore similar to previously reported TMDs and prior measurements on GaAs quantum wells. With increasing temperature, we have to deal not only with the increased dephasing rate, but also with a dramatic suppression of the FWM signal amplitude, such that we are unable to retrieve T_2 above 130 K.

4 Population dynamics

We now move to the pulse sequence depicted in Fig. 3 (top): the first two beams generate a temporal density grating in a material, which is then converted into the FWM signal by the last arriving beam. In this sequence, we thus probe the dynamics of excitons resonantly injected into the light cone. The result is presented in Fig. 3. As in recent works^{23–25}, the data are modeled as a coherent superposition of several complex exponential decays. In our case, two processes are sufficient to describe the observed dynamics: the initial ultrafast decay is followed by a longer component. The first component is due to both radiative decay and non-radiative exciton scattering out of the light cone, the second component describes the effective secondary scattering of dark excitons back into the light cone. The trion's radiative lifetime is expected to be significantly longer than the exciton's one, as was also measured experimentally²⁵. Here instead, the first fast decay component for the trion is barely $\tau_{1,TR} = 0.52\text{ps}$ therefore indicating a prominent non-radiative decay channel. An ultrafast initial decay of the neutral exciton $\tau_{1,EX} = 0.14\text{ps}$, at the limit of the temporal resolution of the experiment, also points toward the existence of a fast non-radiative recombination channel.

5 Coherent imaging and correlations

In this last section, we discuss the coherent spatial imaging of the sample. The time-integrated FWM map, spanning across a large area of $(36 \times 72) \mu\text{m}^2$ is shown in Fig. 4 a). Let us remind that the MoSe₂ covers the entire sample. We however observe that the coherent response is uniquely generated at the hBN flakes, we also distinguish a decreased FWM signal along the discontinuities in the hBN flake, and virtually no signal from the material deposited on the SiO₂. Furthermore, we noticed that no FWM is generated at the thick hBN flakes, with increased roughness and no well defined atomic terraces. The presence of the atomically flat surface, as provided by thin hBN flakes, is therefore essential to perform a successful epitaxy and to carry out coherent spectroscopy reported here. The hyperspectral imaging allows us to determine the central energy of the FWM spectrum. We find that the exciton peak position is centered at 1652.5 meV and is remarkably homogeneous with a standard deviation (FWHM) of 0.87 meV across the entire flake¹⁷.

We carry on by performing a high resolution FWM image (employing a raster scanning step size of $0.2 \mu\text{m}$), around the spot at which the temporal dynamics was measured. In Fig. 4 b) we notice a strong variation of the FWM signal's amplitude. Having access to time-resolved FWM, we can map out σ , and plot it in Fig. 4 c). In agreement with recent studies^{24,26}, we find correlations between the FWM amplitude, linked with the transition oscillator strength, and σ , reflecting the disorder: a stronger FWM signal is detected at the areas with a lower inhomogeneous broadening, as marked with yellow circles. Similar correlations were also found on neighbouring hBN flake on the same sample, further supporting our claim, see Supplementary Fig. 7. Other correlations, between the FWM amplitude and parameters provided by the AFM measurements (height of the hBN terraces, spatial density and orientation of the monolayers) were not detected. However, a decrease of the FWM signal is observed along the hBN cracks.

6 Conclusions & outlook

We have demonstrated a robust coherent nonlinear optical response of MBE-grown MoSe₂ monolayers. By exploiting FWM signal in the temporal domain we have measured dephasing of exciton complexes and ascertained their dephasing via temperature dependence studies. Our results show that these epitaxial monolayers, which could be compatible with the semiconductor optoelectronics industry if grown on wafer-size epitaxial hBN, already display excellent optical response. This however is promoted by their crystallisation on atomically flat surfaces, here provided by exfoliated hBN flakes. The quality and intensity of their coherent nonlinear optical response is comparable with their non-encapsulated counterparts obtained via exfoliation.

A versatility of the MBE growth opens new research avenues for these materials. For example, Janus architecture²⁷ or Mo_xW_{1-x}Se₂ alloys with a well controlled stoichiometry, can be fabricated. Such a technology could be employed to grow magnetic two-dimensional materials, like CrSBr. By exploiting a strong spin-orbit interaction in TMDs monolayers, with controlled doping (for example with vanadium atoms), one can obtain a fer-

romagnetic semiconductor operating at room temperature^{28–30}. These layers could also be embedded into microcavities and serve as excitonic work-bench in polaritonics. Furthermore, with lateral structurization one could introduce in-plane confinement and manufacture quantum dot or quantum wires, permitting to explore the physics of edge states.

Surprisingly, the epitaxial growth via CVD has recently been employed to understand the surface reconstruction mechanisms during the formation of moiré quantum matter^{31,32}. In that context, we believe that combining the MBE-growth of transition metal dichalcogenies homo- and hetero-bilayers with nonlinear spectroscopy could yield intriguing findings, within the crossover of material science at the nanoscale and their light-matter interaction.

7 Acknowledgements

We gratefully acknowledge the financial support from projects no. 2020/39/B/ST3/03251 and 2021/41/B/ST3/04183 financed by the National Science Centre (Poland), "Tandem for Excellence" IDUB scheme at the University of Warsaw and EU Graphene Flagship. J.K. acknowledges the support of TU Munich through the Global Invited Professorship Program 2021-2023. M.P. acknowledges support by the Foundation for Polish Science (MAB/2018/9 Grant within the IRA Program financed by EU within SG OP Program). K.W. and T.T. acknowledge support from the Elemental Strategy Initiative conducted by the MEXT, Japan, (grant no. JPMXP0112101001), JSPS KAKENHI (grant no. JP20H00354), and the CREST (JPMJCR15F3), JST. We thank Daniel Wigger for his comments on the manuscript.

8 Author Contributions

The epitaxial growth of MoSe₂ samples was performed by K.P. and W.P.. The hBN crystals were grown by T.T. and K.W.. The AFM imaging was carried out by S.L-D.. The spectroscopy and data analysis were performed by J.K. and K.P.. The project was initiated and supervised by P.K., M.P. and W.P.. The paper was written by J.K. and W.P.. All authors discussed the results and commented on the manuscript.

9 Conflicts of interest

There are no conflicts to declare.

Notes and references

- 1 K. S. Novoselov, A. K. Geim, S. V. Morozov, D. Jiang, Y. Zhang, S. V. Dubnisi, I. V. Grigorieva and A. A. Firsov, *Science*, 2004, **306**, 666–669.
- 2 T. Smoleński, P. E. Dolgirev, C. Kuhlenskamp, A. Popert, Y. Shimazaki, P. Back, X. Lu, M. Kroner, K. Watanabe, T. Taniguchi, I. Esterlis, E. Demler and A. Imamoğlu, *Nature*, 2021, **595**, 53–57.

- 3 D. Huang, J. Choi, C.-K. Shih and X. Li, *Nat. Nanotech.*, 2022, **17**, 227–238.
- 4 A. Popert, Y. Shimazaki, M. Kroner, K. Watanabe, T. Taniguchi, A. Imamoğlu and T. Smoleński, *Nano Letters*, 2022, **22**, 7363–7369.
- 5 A. Chernikov, T. C. Berkelbach, H. M. Hill, A. Rigosi, Y. Li, O. B. Aslan, D. R. Reichman, M. S. Hybertsen, and T. F. Heinz, *Phys. Rev. Lett.*, 2014, **113**, 076802.
- 6 A. Sāynājoki, L. Karvonen, H. Rostami, A. Autere, S. Mehravar, A. Lombardo, R. A. Norwood, T. Hasan, N. Peyghambarian, H. Lipsanen, K. Kieu, A. C. Ferrari, M. Polini and Z. Sun, *Nat. Commun.*, 2017, **8**, 893.
- 7 H. Liu, Y. Li, Y. S. You, S. Ghimire, T. F. Heinz and D. A. Reis, *Nat. Phys.*, 2017, **13**, 262–265.
- 8 G. Moody, C. K. Dass, K. Hao, C.-H. Chen, L.-J. Li, A. Singh, K. Tran, G. Clark, X. Xu, G. Berghäuser, E. Malic, A. Knorr and X. Li, *Nat. Commun.*, 2015, **6**, 8315.
- 9 T. Jakubczyk, V. Delmonte, M. Koperski, K. Nogajewski, C. Faugeras, W. Langbein, M. Potemski and J. Kasprzak, *Nano Letters*, 2016, **16**, 5333–5339.
- 10 F. H. L. Koppens, T. Mueller, P. Avouris, A. C. Ferrari, M. S. Vitiello and M. Polini, *Nat. Nanotech.*, 2014, **9**, 780–793.
- 11 D. Kalita, V. Bouchiat, L. Marty and N. Bendib, *Patent*, 2021.
- 12 K. Ludwiczak, A. K. Dąbrowska, J. Binder, M. Tokarczyk, J. Iwański, B. Kurowska, J. Turczyński, G. Kowalski, R. Bożek, R. Stępniewski, W. Pacuski and A. Wyszomolek, *ACS Applied Materials & Interfaces*, 2021, **13**, 47904–47911.
- 13 X. Wang, Y. Gong, G. Shi, W. L. Chow, K. Keyshar, G. Ye, R. Vajtai, J. Lou, Z. Liu, E. Ringe, B. K. Tay and P. M. Ajayan, *ACS Nano*, 2014, **8**, 5125–5131.
- 14 S. Shree, A. George, T. Lehnert, C. Neumann, M. Benelajla, C. Robert, X. Marie, K. Watanabe, T. Taniguchi, U. Kaiser, B. Urbaszek and A. Turchanin, *2D Materials*, 2019, **7**, 015011.
- 15 M.-W. Chen, D. Ovchinnikov, S. Lazar, M. Pizzochero, M. B. Whitwick, A. Surrente, M. Baranowski, O. L. Sanchez, P. Gillet, P. Plochocka, O. V. Yazyev and A. Kis, *ACS Nano*, 2017, **11**, 6355–6361.
- 16 C. Vergnaud, M. Gay, C. Alvarez, M.-T. Dau, F. Pierre, D. Jalabert, C. Licitra, A. Marty, C. Beigné, B. Grévin, O. Renault, H. Okuno and M. Jamet, *2D Materials*, 2019, **6**, 035019.
- 17 W. Pacuski, M. Grzeszczuk, K. Nogajewski, A. Bogucki, K. Oreszczuk, J. Kucharek, K. E. Polczyńska, B. Seredyński, A. Rodek, R. Bożek, T. Taniguchi, K. Watanabe, S. Kret, J. Sadowski, T. Kazimierzczuk, M. Potemski and P. Kossacki, *Nano Letters*, 2020, **20**, 3058–3066.
- 18 W. Langbein and B. Patton, *Optics Letters*, 2006, **31**, 1151–1153.
- 19 A. Esser, E. Runge, R. Zimmermann and W. Langbein, *Phys. Rev. B*, 2000, **62**, 8232–8239.
- 20 F. Rana, O. Koksai, M. Jung, G. Shvets and C. Manolatu, *Phys. Rev. B*, 2021, **103**, 035424.
- 21 C. Boule, D. Vacklavkova, M. Bartos, K. Nogajewski, L. Zdražil, T. Taniguchi, K. Watanabe, M. Potemski and J. Kasprzak, *Phys. Rev. Mater.*, 2020, **4**, 034001.
- 22 T. Jakubczyk, K. Nogajewski, M. R. Molas, M. Bartos, W. Langbein, M. Potemski and J. Kasprzak, *2D Mater.*, 2018, **5**, 031007.
- 23 L. Scarpelli, F. Masia, E. M. Alexeev, F. Withers, A. I. Tartakovskii, K. S. Novoselov and W. Langbein, *Phys. Rev. B*, 2017, **96**, 045407.
- 24 T. Jakubczyk, G. Nayak, L. Scarpelli, F. Masia, W.-L. Liu, S. Dubey, N. Bendib, L. Marty, T. Taniguchi, K. Watanabe, G. N. J. Coraux, V. Bouchiat, W. Langbein, J. Renard and J. Kasprzak, *ACS Nano*, 2019, **13**, 3500–3511.
- 25 A. Rodek, *2D Materials*, 2023, accepted, arXiv:2302.13109.
- 26 T. L. Purz, E. W. Martin, W. G. Holtzmann, P. Rivera, A. Alfrey, K. M. Bates, H. Deng, X. Xu and S. T. Cundiff, *The Journal of Chemical Physics*, 2022, **156**, 214704.
- 27 M. M. Petrić, M. Kremser, M. Barbone, Y. Qin, Y. Sayyad, Y. Shen, S. Tongay, J. J. Finley, A. R. Botello-Méndez and K. Müller, *Phys. Rev. B*, 2021, **103**, 035414.
- 28 L.-A. T. Nguyen, K. P. Dhakal, Y. Lee, W. Choi, T. D. Nguyen, C. Hong, D. H. Luong, Y.-M. Kim, J. Kim, M. Lee, T. Choi, A. J. Heinrich, J.-H. Kim, D. Lee, D. L. Duong, and Y. H. Lee, *ACS Nano*, 2021, **15**, 20267–20277.
- 29 S. J. Yun, B. W. Cho, T. Dinesh, D. H. Yang, Y. I. Kim, J. W. Jin, S.-H. Yang, T. D. Nguyen, Y.-M. Kim, K. K. Kim, D. L. Duong, S.-G. Kim and Y. H. Lee, *Adv. Materials*, 2022, **34**, 2106551.
- 30 P. Mallet, F. Chiapello, H. Okuno, H. Boukari, M. Jamet and J.-Y. Veuillen, *Phys. Rev. Lett.*, 2020, **125**, 036802.
- 31 Zhao, *arXiv:2202.11139*.
- 32 Li, *arXiv:2212.07686*.

10 Supplementary Figures:

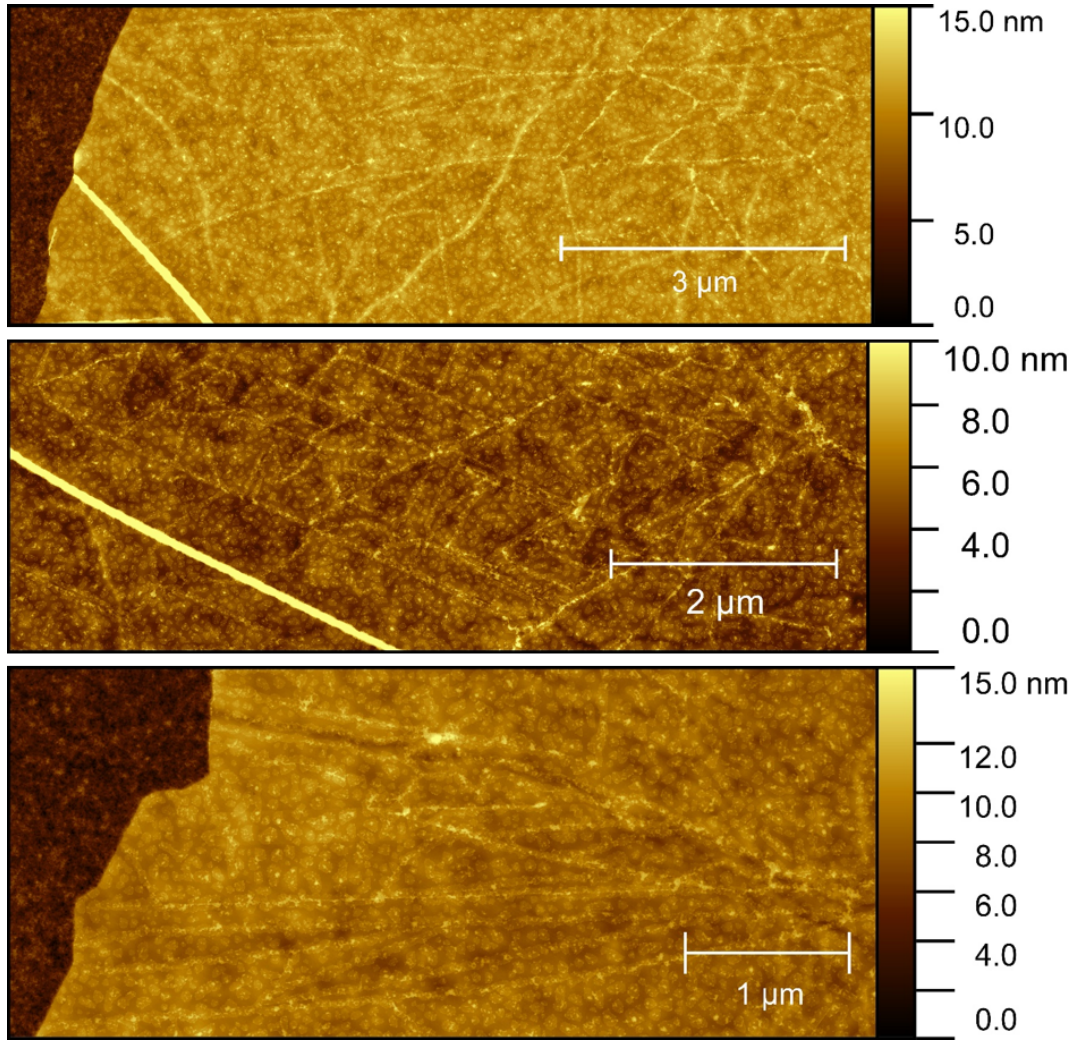


Fig. 5 AFM imaging of the investigated sample. The scale is given by horizontal bars, respectively. The MoSe₂ grows on the surface of the hBN: one can distinguish monolayer flakes, bilayers, and areas not yet covered by the MoSe₂. The characteristic stripes, which are building up on a few micron scale, could be due to the surface reconstruction mechanism.

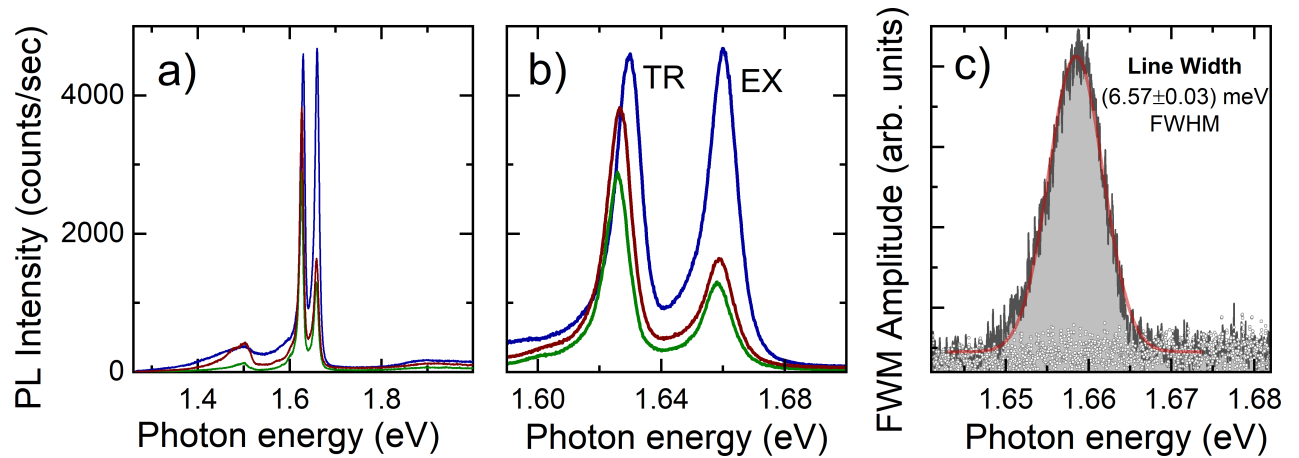


Fig. 6 Complementary PL and FWM spectra. a) Typical micro-photoluminescence (PL) spectra of the investigated sample excited by a CW laser at 532 nm at $T=10$ K. The spectra are dominated by narrow exciton and trion lines with their relative intensities depending on the underlying residual doping. Note a quasi-constant center transition energy indicating lack of strain. A defect band is also visible at the low energy side, as in bare TMD monolayers obtained via mechanical exfoliation. b) as in a) but zoomed into the spectral region of exciton and trion transitions. A typical line width of 10 meV FWHM is measured. c) Spectrally-resolved FWM amplitude measured at $\tau_{12}=0.5$ ps and $\tau_{23}=0$. Locally the FWM line width as narrow as 6.6 meV is measured, indicating comparable homogeneous and inhomogeneous contributions to the spectral line shape. Open circles indicate the noise level.

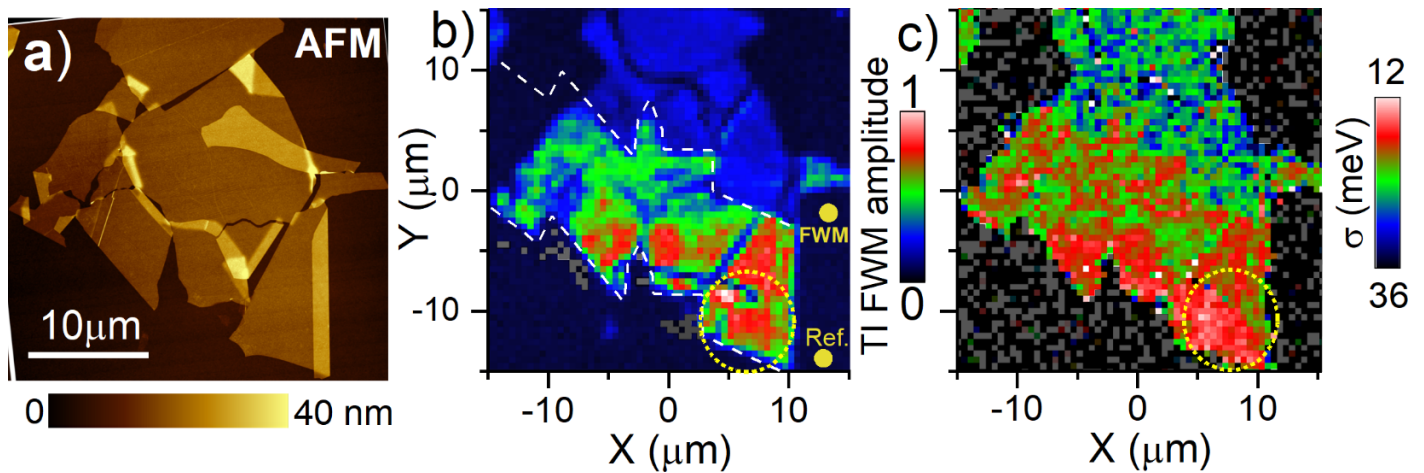
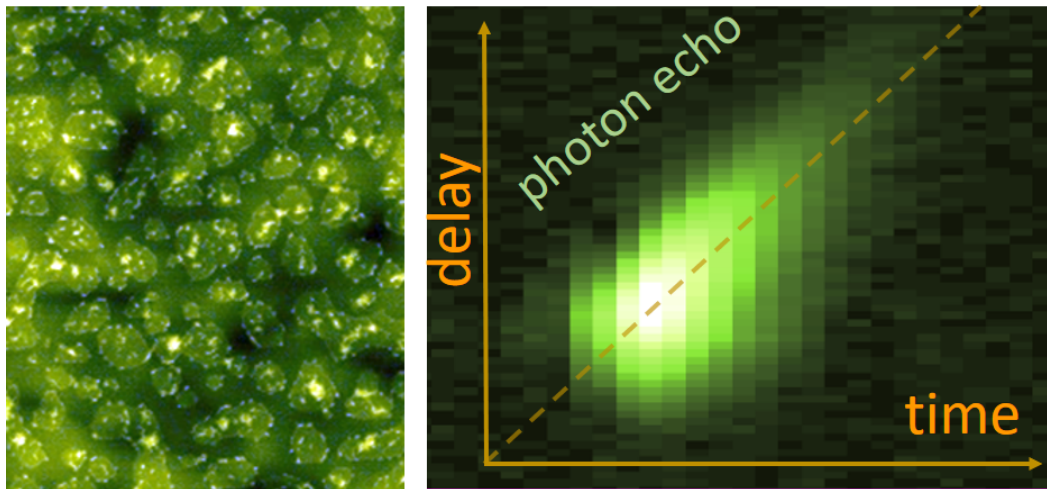


Fig. 7 FWM imaging and correlations between FWM amplitude and inhomogeneous broadening.. A complementary set of data to those shown in Fig. 4, but obtained on a different hBN flake, as shown in the AFM image in a). The corresponding imaging of the FWM amplitude is shown in b). It is anti-correlated with the inhomogeneous broadening σ shown in c): the strongest FWM signal corresponds to the lowest σ , as indicated with the dotted yellow circle. In b), we observe a significantly weaker FWM signal at the upper part of the flake compared to the lower area. We notice that the form of this boundary faithfully mimics the shape of hBN edge at the bottom of the flake, as indicated by white dashed lines. Let us note that the reference's intensity drops significantly when reflecting from the hBN, compared to the SiO_2 substrate. Hence, the generated amplitude of the FWM spectral interference is lowered when the reference pulse impinges the hBN flake. This effect is thus due to the signal detection arrangements, and not due to intrinsic sample properties.



By performing ultrafast nonlinear spectroscopy we assess optical coherence of MoSe_2 monolayers grown by molecular beam epitaxy.

Fig. 8 Table of Contents entry. Left: Atomic force microscopy image showing MBE grown MoSe_2 studied in this work. The flakes, with their typical size of 100 nm, are dominated by monolayers, with bilayers starting to be formed on top of monolayers. The growth was terminated before the coalescence of the flakes. Right: A typical time-resolved four-wave mixing response, exhibiting photon echo. By inspecting photon echos we evaluate homogeneous and inhomogeneous broadenings of excitons complexes present in the optical spectra.